1 **Paired organic matter and pyrite δ^{34}S records reveal mechanisms of carbon, sulfur,**
2 **and iron cycle disruption during Ocean Anoxic Event 2**
3
4 Morgan Reed Raven[*a,b], David A. Fike [b], Alexander S. Bradley [b]; Maya L. Gomes[c],
5 Jeremy D. Owens [d], Samuel A. Webb [e]
6

7 [a] *Dept. of Earth Sciences, University of California, Santa Barbara, CA 93130 USA*
8 [b] *Dept. of Earth and Planetary Sciences, Washington University in St Louis, MO 63130*
9 [c] *Dept. of Earth and Planetary Sciences, Johns Hopkins University, Baltimore, MD 21218*
10 [d] *Dept. of Earth, Ocean, and Atmospheric Science, Florida State University, Tallahassee, FL*
11 *32306*
12 [e] *Stanford Synchrotron Radiation Lightsource, Stanford University, Menlo Park, CA, 94025*
13 ** = corresponding author, raven@ucsb.edu*
14

15   **Abstract**

16   Sulfur (S) isotope compositions of pyrites in the sedimentary record have played an

17   important part in our understanding of biogeochemical cycling in the geologic record.

18   However, the kinetics of pyritization are complex and depend strongly on the reactivity

19   and mineralogy of available iron. As a second major sink for sulfide in anoxic sediments,

20   organic matter (OM) provides essential context for reconstructing the distribution and

21   isotopic composition of environmental sulfide. To first order, roughly parallel pyrite and

22   OM δ^{34}S profiles reflect changes in sulfide, while independent patterns require alternative

23   explanations, including changes in iron availability or OM characteristics. We apply this

24   framework to Ocean Anoxic Event 2 (OAE-2, 94 Mya), a period of enhanced reduced C

25   and S burial (in OM and pyrite) that was associated with expanded marine anoxia. We

26   present paired S-isotope records for pyrite and OM along with profiles of OM S:C ratio

27   and S redox speciation from four well-characterized lithologic sections (Pont d'Issole,

28   Cismon, Tarfaya Basin, and Demerara Rise) to reconstruct both local redox structure and

29   global mechanisms impacting the C, S and Fe cycles around OAE-2.

30

31   OM sulfurization appears to be a major control on OM preservation at all four sites.

32   Similar to modern anoxic environments, there is a positive correlation between OM S:C

33   ratios and OM concentrations for sites with more reducing conditions, implying a link

34   between OM sulfurization and burial. At consistently anoxic sites like Tarfaya Basin and

35   Demerara Rise, strongly sulfurized OM with a consistent S redox speciation and S-

36   isotope composition most likely formed rapidly in sinking particles before, during, and

37   after OAE-2. Particle-hosted OM sulfurization may therefore have been a central

38   mechanism facilitating the massive burial of OM in anoxic environments during this and

39   other periods of enhanced global carbon burial. At the same time, a nearly 25‰ negative

40   shift in the $\delta^{34}S$ values of pyrite – but not OM – occurs at multiple, globally distributed

41   sites near the onset of OAE-2, indicating slower pyritization reactions that likely reflect

42   changes in iron delivery due to expanding regional or global anoxia. The combination of

43   pyrite and organic S isotopes thus provides novel constraints on the interwoven cycles of

44   carbon, iron, and sulfur across a major carbon cycle perturbation.

45

46   **Introduction**

47   Ocean Anoxic Event 2 (OAE-2, also termed the Cenomanian–Turonian Boundary Event)

48   was a period of dynamic changes in the global carbon cycle in the Cretaceous (~94

49   million years ago, Mya) during which a large portion of the global ocean experienced

50   anoxia (Ostrander et al., 2017) and associated biological turnover (Keller et al., 2008) and

51   refs therein). Expanded euxinia at the onset of the event contributed to the preservation of

52   extraordinary amounts of organic matter (OM) in marine sediments, equivalent to

53   roughly a 60 to 80% increase in the global flux maintained for ~500,000 years (Owens et

54   al., 2013; 2018; Sageman et al., 2006). This burst of ^{13}C-depleted OM preservation

55   generated the characteristic positive C-isotope excursion for OAE-2 and substantially

56   drew down atmospheric CO_2 (Jarvis et al., 2011). OM sulfurization can enhance the

57   preservation of OM under anoxic conditions (Boussafir et al., 1995) and has been

58   described in TOC–rich (>10 wt%) OAE-2 shales (Hetzel et al., 2009; Kolonic et al.,

59   2002) as well as in interbedded carbonates and marly shales with more moderate (0.2–3

60   wt%) TOC (Raven et al., 2018). Still, it remains difficult to quantify the impact of

61 sulfurization on OM preservation under different environmental conditions, much less to

62 extrapolate to global fluxes of reduced sulfur and carbon burial or to estimate how those

63 fluxes might change before, during, and after OAE-2.

64

65 Primary considerations for determining the significance of sulfurization for C fluxes are

66 the rates and locations of S cycling in the environment. Two distinct timescales of

67 sulfurization reactions occur in modern environments: gradual sulfurization reactions

68 between bisulfide (HS^-) and relatively recalcitrant OM occur over thousands of years

69 under strongly reducing conditions (Werne et al., 2000), and rapid sulfurization reactions

70 between polysulfides (S_x^{2-}) and relatively fresh, labile OM occur on timescales of days

71 near dynamic redox interfaces, for example in sinking particles (Raven et al., 2016a).

72 Rapid sulfurization has the potential to impact a much larger pool of OM and have a

73 much more dramatic impact on C fluxes (Raven et al., 2018).

74

75 S–isotope ratios (expressed as $\delta^{34}S$ values) are powerful tools for reconstructing the

76 sources of sulfide in the environment as well as its various potential sinks, including

77 reoxidation or precipitation as either abiogenic OM or pyrite (FeS_2). Near the onset of

78 OAE-2, previously published S-isotope profiles of pyrite from multiple sites show

79 intriguing shifts toward ^{34}S-depleted values that have been interpreted in terms of

80 changing marine sulfate concentrations (Adams et al., 2010), local chemocline position

81 (Gomes et al., 2016), and the extent of oxidative microbial sulfur cycling (Hetzel et al.,

82 2009; Kolonic et al., 2002). Although each of these hypotheses invoke changes in the

83 distribution or $\delta^{34}S$ value of sulfide in the environment, OAE-2 is also associated with

84   major changes in iron cycling due to inputs from active rifting and volcanism (Owens et

85   al., 2012), which could also impact pyrite δ^{34}S values via changes in iron distributions

86   and mineralogy. To distinguish among these possibilities, we integrate pyrite δ^{34}S records

87   with OM δ^{34}S values and S speciation data from four OAE-2 sections located in different

88   parts of the Tethys and proto–North Atlantic Oceans. Our results indicate that the strong

89   negative shift in pyrite δ^{34}S values from globally dispersed sites likely reflects a change

90   in the quantity or speciation of iron delivery to these locations. We also find evidence for

91   a generalizable relationship between sulfurization intensity and OM preservation in

92   sediments, which implies that OM sulfurization can be a primary driver of changes in C

93   burial during OAE-2 and throughout Earth history.

94

95   **Methods Summary**

96   Samples were prepared from previously sampled sections by sequential extraction

97   (Canfield et al., 1986; Raven et al., 2018). Powdered rock samples were washed with DI

98   water, lyophilized, and microwave–extracted twice with organic solvents (9:1

99   dichloromethane:methanol, MARS6, CEM Corp.) prior to chromium reduction (6N HCl

100 + CrCl$_2$, 180°C, 4 hrs) and trapping of released sulfide as ZnS in 5% zinc acetate

101 solution. The microwave extraction step removed organic-solvent soluble S, which was

102 not further analyzed for this study. The S liberated by chromium reduction is an

103 operationally-derived pool of metal sulfides, typically considered to be primarily

104 composed of pyrite, and thus will be referred to as 'pyrite' here. Washed ZnS solids from

105 the chromium reduction were oxidized with 30% H$_2$O$_2$ (24°C, 24 hrs), quantified as

106 sulfate by ion chromatography (Metrohm 881 ion chromatograph with a Metrosep A

107   Supp 7 150 x 4.0 mm anion column) and then precipitated as $BaSO_4$ with barium chloride

108   for S-isotope analysis by combustion EA-IRMS (Costech 4010 EA coupled to a Thermo

109   Delta V Plus, configured for S). Remaining solids after chromium reduction were also

110   analyzed by EA-IRMS for S concentrations and $\delta^{34}S$ values. Organic C concentrations

111   and $\delta^{13}C$ values were measured using a Thermo Flash 2000 EA with zero-blank

112   autosampler coupled to a Delta V Plus, configured for C. All C- and S-isotope ratio

113   measurements were made at Washington University in St Louis and are reported in per

114   mil (‰) units relative to VPDB and VCDT, respectively. Unconsolidated sediments from

115   a recent (160,000 – present) core from the TOC-lean Gulf of Lion (northwestern

116   Mediterranean, borehole PRGL1–4, https://www.pangaea.de/?q=PROMESS1) were

117   prepared according to the same methods for comparison below. Residual solids were also

118   analyzed for organic S speciation by x-ray absorption spectroscopy on beamline 14–3 at

119   the Stanford Synchrotron Radiation Lightsource (SSRL) at the SLAC National

120   Accelerator Laboratory. Spectra were collected for each sample using a ~500 x 1000 μm

121   beam with a flux of 2 x 10^{10} photons/sec, calibrated to the thiosulfate ($Na_2S_2O_3$) pre-edge

122   peak at 2472.02 eV. Spectra were processed and fit using a set of in-house standards with
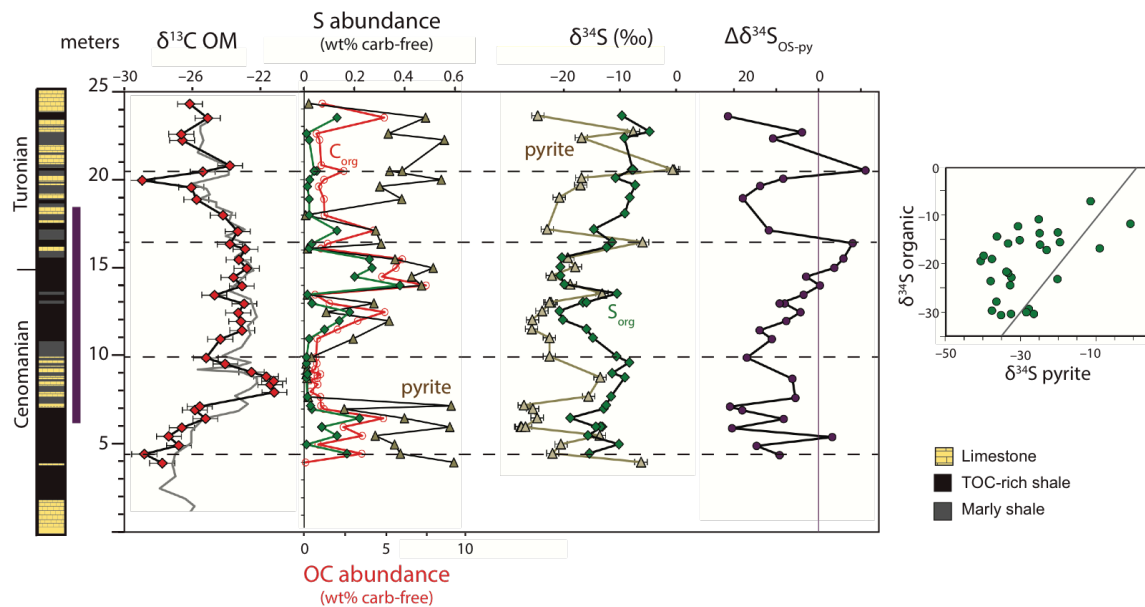
123   the SIXPACK software package (Webb, 2005).

124

125   **Study Sites and Results**

126
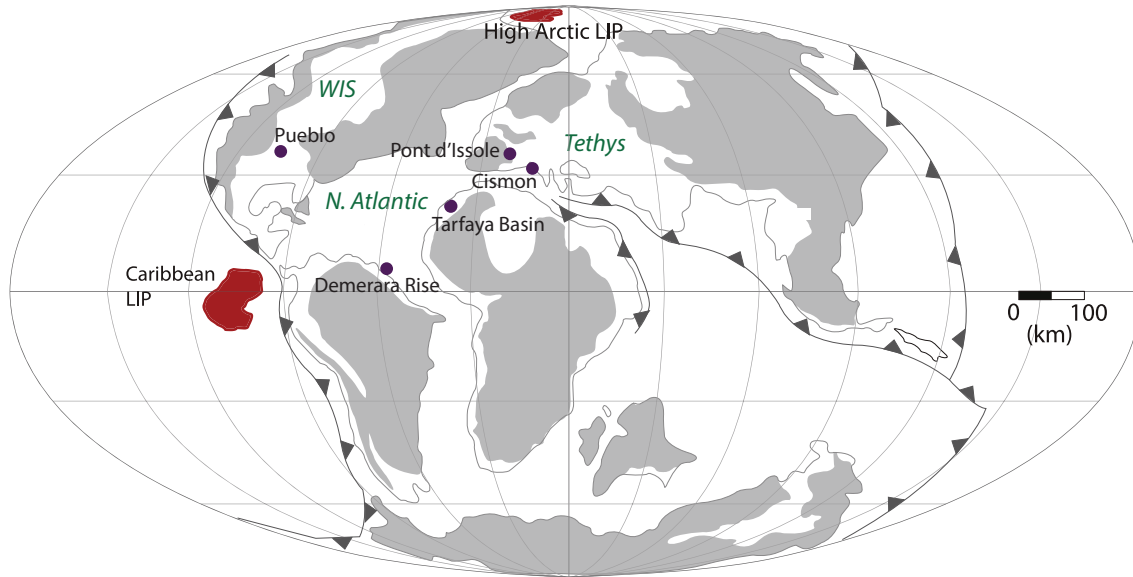
Fig. 1 Paleo-geography of study sites during OAE-2. Map is modified from (du Vivier et al., 2014) with study sections marked by purple circles. Locations of Large Igneous Provinces (LIP) are also shown in red.

130

131

Fig. 2 Pont d'Issole record. The purple bar at left represents the interpreted duration of OAE-2 based on the C-isotope excursion. The grey line for $\delta^{13}C_{OM}$ is from (Jarvis et al.,

134   2011), and lithology is from (Gomes et al., 2016). Dashed horizontal lines are intended as

135   visual aids to highlight patterns in the records. Vertical purple line for $\Delta\delta^{34}S_{OS-py}$ shows

136    $\delta^{34}S_{pyrite} = \delta^{34}S_{OS}$. Grey line in the right-hand panel shows a 1:1 line.

137

138   The Pont d'Issole section was deposited in a subsiding basin within the northern Tethys

139   Ocean (~30°N, Fig. 1) in several hundred meters of water depth with an average

140   sedimentation rate of roughly 2.4 cm/yr (12-m-thick C-isotope excursion, ~500 kyr,

141   (Jarvis et al., 2011)). This section is characterized by recurrent shifts in lithology and OM

142   concentration between relatively OM-lean (<0.2 wt% TOC) limestones and relatively

143   OM-rich (>1.0 wt% TOC) shales and marly shales (Gomes et al., 2016). Shale layers

144   contain relatively S-rich and ^{34}S-depleted OM, indicating early OM sulfurization during

145   shale deposition under more O_2-limited conditions (Raven et al., 2018). The pyrite δ^{34}S

146   record from our Pont d'Issole sample set (Fig. 2; cf. (Gomes et al., 2016)) has many

147   similarities to the OM δ^{34}S record, with comparable shifts toward lower δ^{34}S values in

148   shales before and during the OAE-2 C-isotope excursion. There are also instances,

149   however, where the S-isotope composition of pyrite behaves independently from OM: at

150   5.5 m and 20.5 m, for example, pyrite is locally strongly ^{34}S-enriched without any

151   parallel excursion in OM δ^{34}S. Additionally, the δ^{34}S offset between pyrite and organic

152   matter (Fig. 2, $\Delta\delta^{34}S_{OS-py}$) decreases systematically from 17.4 to −7.9‰ across the

153   duration of the C-isotope excursion. OM and pyrite δ^{34}S values thus show significant

154   spread around and to the left of the 1:1 line in the cross-plot in Figure 2.

155

156   At Cismon, a narrow, ~35-cm-thick layer of OM-rich (6.5 – 21.4 wt% TOC) black shale

157   corresponds to part of the OAE-2 C-isotope excursion, although major portions of the C-

158   isotope excursion are absent due to hiatuses (Gambacorta et al., 2015; Gomes et al.,

159   2016). On either side of this lithologic unit, corresponding to the Bonarelli Layer, rocks

160   from Cismon are bedded layers of OM-lean (≤ 0.05 wt% TOC), micritic foraminiferal

161   limestones with occasional cherts and grey shales (Bellanca et al., 1996a; Gambacorta et

162   al., 2015). Unfortunately, these limestones are generally too OM-lean and silicate-rich to

163   permit spectroscopic analysis of S speciation or isotopic analysis of organic S by

164   conventional EA-IRMS. For a point of comparison with OAE-2 shales, we analyzed a

165   selection of limestones with 0.1–0.7 wt% TOC from lower in the section, representing

166   approximately 96 – 100 Mya (spanning a 20-meter-thick zone from 37.5 m above the

167   OAE-1a C-isotope excursion to 20 m below the onset of OAE-2). In both the TOC-rich

168   layer and earlier TOC-lean limestones, OM from Cismon is strongly ^{34}S-depleted, with

169   δ^{34}S values averaging –37‰ during OAE-2 and –38.8‰ in the earlier samples. Pyrite is

170   also very strongly ^{34}S-depleted throughout the section, averaging –42.7‰ during OAE-2

171   and –49‰ in the earlier samples (Gomes et al., 2016).

172
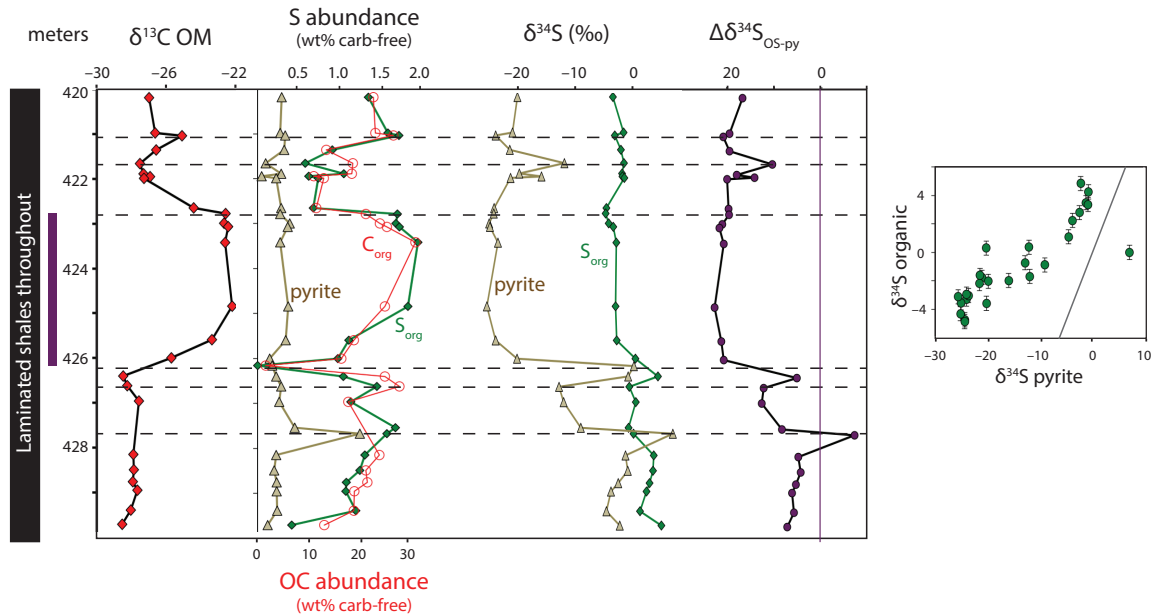
Fig. 3 Demerara Rise record. The purple bar at left represents the interpreted duration of OAE-2 based on the C-isotope excursion. Dashed horizontal lines are intended as visual aids to highlight patterns in the records. Vertical purple line for $\Delta\delta^{34}S_{OS-py}$ shows $\delta^{34}S_{pyrite} = \delta^{34}S_{OS}$. Grey line in the right-hand panel shows a 1:1 line.

Sediments from Demerara Rise (ODP 1258, using modified composite depths after (Erbacher et al., 2005)) were deposited in the western tropical proto-North Atlantic Ocean and are generally described as laminated OM-rich marl to black shales throughout the investigated section, with an apparent average sedimentation rate of ~0.8 cm/kyr for the 3.5-m-thick C-isotope excursion (Owens et al., 2016). On a carbonate-free basis, concentrations of OM, organic S, and pyrite S are largely invariant across the onset and termination of the OAE. Due to reduced carbonate concentrations during the C-isotope excursion, there is a perceived increase in pyrite and OM concentrations across this interval on a whole-rock basis ((Hetzel et al., 2009); Supplemental Fig. 1). Sediments are extremely OM-rich (Erbacher et al., 2005; Hetzel et al., 2009), containing an average of

189 24 wt% organic C (Fig. 3, (Owens et al., 2016)) and 4.1 wt% organic S on a carbonate-

190 free basis. These concentrations of organic S exceed those of pyrite S by roughly five

191 times. OM δ^{34}S values are also broadly invariant; samples after the onset of the OAE are

192 slightly more ^{34}S-depleted, but all OM δ^{34}S values fall in a relatively narrow range

193 between –4.9‰ and +4.8‰. In contrast, pyrite δ^{34}S values decline substantially across

194 the 2 m of section leading up to the onset of OAE-2, from around –3‰ to around –25‰,

195 in agreement with previously published data (Hetzel et al., 2009). Pyrite S-isotopes are

196 relatively stable at these moderately ^{34}S-depleted compositions throughout the OAE-2 C-

197 isotope excursion and recover partly after the termination of the event. Accordingly,

198 $\Delta\delta^{34}$S$_{OS-py}$ at Demerara Rise increases from ~6‰ prior to OAE-2 to ~21‰ during the

199 OAE-2 C-isotope excursion, and the slope of the data in a pyrite–OM δ^{34}S crossplot is

200 much shallower than the 1:1 line. Like at Pont d'Issole, there are also instances of locally

201 ^{34}S-enriched pyrite without similar enrichment in OS (e.g., 427.7 m).

202

203

11
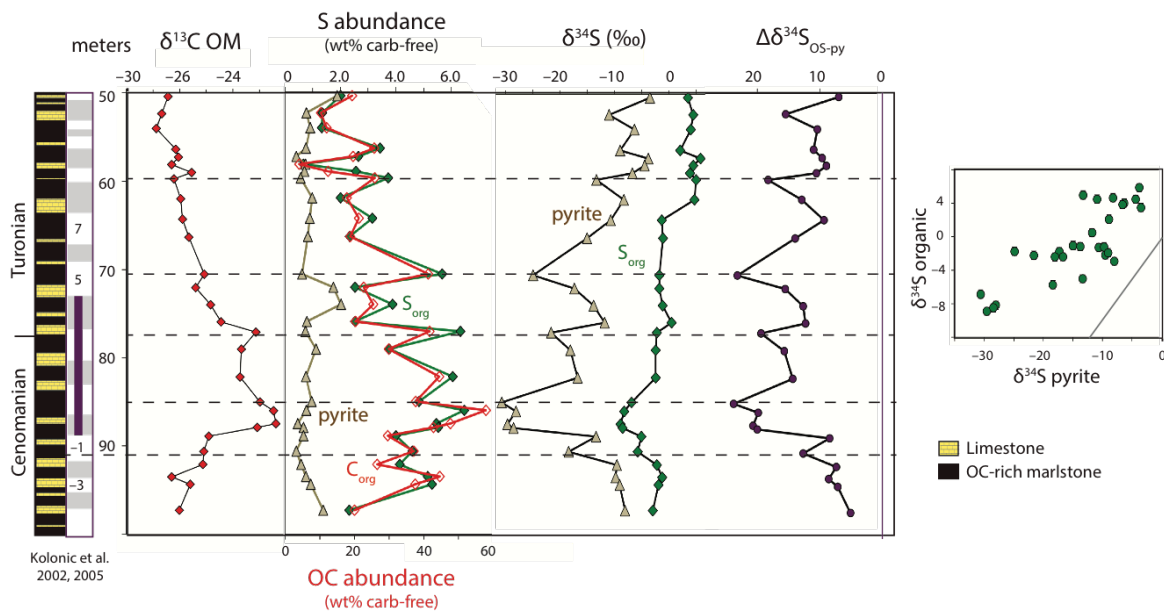
204 **Fig. 4 Tarfaya Basin record.** Lithology is shown at left, paired with recurrent

205 sedimentary cycles from Kolonic (2002, 2005). Dashed horizontal lines indicate depths

206 with relatively abundant OM and ^{34}S-depleted pyrite. The purple bar at left represents the

207 interpreted duration of OAE-2 based on the C-isotope excursion. Vertical purple line for

208 $\Delta\delta^{34}S_{OS-py}$ shows $\delta^{34}S_{pyrite} = \delta^{34}S_{OS}$. Grey line in the right-hand panel shows a 1:1 line.

209

210 Tarfaya Basin sediments (sampled from Shell exploration core S75) were deposited on

211 the outer shelf of northwest Africa during a series of transgressive cycles associated with

212 rifting of the southern North Atlantic Basin. High productivity and high sedimentation

213 rates (averaging ~3.3 cm/kyr across the 16.5-meter-thick C-isotope excursion; (Kolonic

214 et al., 2005)) supported the formation of extremely OM-rich black shales and somewhat

215 less OM-rich carbonates, which alternate on apparently orbital timescales (Kolonic et al.,

216 2005; 2002; Poulton et al., 2015) (Fig. 4). This variation is also apparent in the δ^{34}S

217 profile of pyrite, which is consistent with lower resolution data from (Kolonic et al.,

218 2002) and Böttcher et al. (unpublished) as reported in (Hetzel et al., 2009). Although we

219 do not have the sampling density to resolve individual orbital cycles, OM-rich layers

220 generally contain relatively ^{34}S-depleted pyrite, as highlighted in dashed lines in Fig. 4.

221 On top of this regular variation, the S-isotope profiles for OM and pyrite have key

222 similarities to those from Demerara Rise. OM and pyrite δ^{34}S values prior to the onset of

223 the OAE are between 0 and –10‰. By the onset of the OAE-2 C-isotope excursion,

224 pyrite δ^{34}S values are at their minimum, generally –30‰. In the upper part of the core

225 (depths < 65 m), post-OAE, pyrite δ^{34}S values return to pre-excursion values (–5 to –

226 10‰). OM δ^{34}S values express a muted drop from near –2‰ to a minimum of –8.9‰ at

227 the onset of OAE-2 and a gradual increase thereafter, reaching ~4‰ in the top of the

228 section.

229

230 **Table 1. Average relative abundances of organic S moieties for sections spanning**

231 **OAE-2 by XAS**

Site	#	S:C	Sulfides		Disulfides		Aromatic S		Sulfoxides		Sulfonates		Sulfate Esters	
			mean	1 s.d.	mean	1 s.d.	mean	1 s.d.	mean	1 s.d.	mean	1 s.d.	mean	1 s.d.
Demerara Rise	24	5.9%	64%	3%	23%	2%	2%	1%	4%	1%	6%	2%	1%	1%
Tarfaya Basin	23	5.0%	59%	3%	14%	3%	14%	1%	4%	1%	8%	1%	0%	0%
Pont d'Issole (S:C >3%)	10	4.3%	57%	3%	17%	2%	15%	2%	3%	1%	8%	2%	0%	1%
Cismon	4	4.8%	52%	2%	16%	2%	20%	1%	4%	1%	7%	1%	1%	0%
Pont d'Issole (S:C <3%)	13	2.2%	42%	8%	22%	8%	16%	8%	3%	2%	11%	7%	5%	5%

232
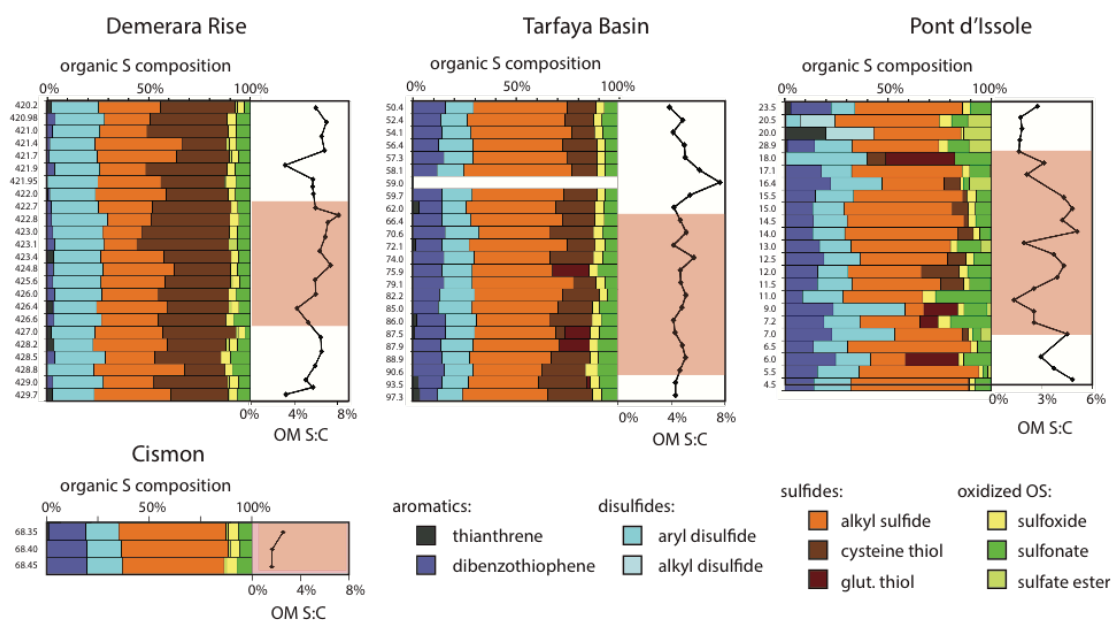
233

234 **Fig. 5:   Organic S speciation in organic matter.** XAS and organic matter S:C

235 (mol/mol) ratios show consistent OS redox speciation among Demerara, Tarfaya, and

236 Cismon samples and variable OS redox speciation associated with local environmental

237 change in Pont d'Issole. The red shaded intervals correspond to the OAE-2 C-isotope

238 excursion at each site. Categories of reduced S structures (aromatic, disulfide, and

13

239 sulfide) can be confidently distinguished, but specific identifications within these groups

240 (e.g., between sulfides and thiols) are tentative.

241

242 X-ray absorption spectroscopy was used to quantify the relative contributions of different

243 forms of organic S to the total solvent– and acid–insoluble OM pool (Eglinton et al.,

244 1994; Vairavamurthy, 1998). At Demerara Rise and Tarfaya Basin, the speciation of OS

245 is remarkably consistent before, during, and after the OAE-2 C-isotope excursion (Fig.

246 5), contrasting the variation observed in the Pont d'Issole profile ((Raven et al., 2018);

247 Fig. 5). Additionally, as summarized in Table 1, the redox speciation of S-rich OM (S:C

248 ≥ 3%) is quite comparable at all four sites, with over half of OS present as alkyl sulfides

249 and substantial amounts of disulfides and sulfonates. There are subtle, yet robust, site-to-

250 site differences in OS speciation, with Demerara Rise OM richer in disulfides and leaner

251 in aromatic S forms than OM from Cismon, Tarfaya Basin, and Pont d'Issole shales. In

252 less strongly sulfurized samples from Pont d'Issole, the relative proportions of oxidized

253 OS forms − sulfonates and sulfate esters − are generally higher at the expense of alkyl
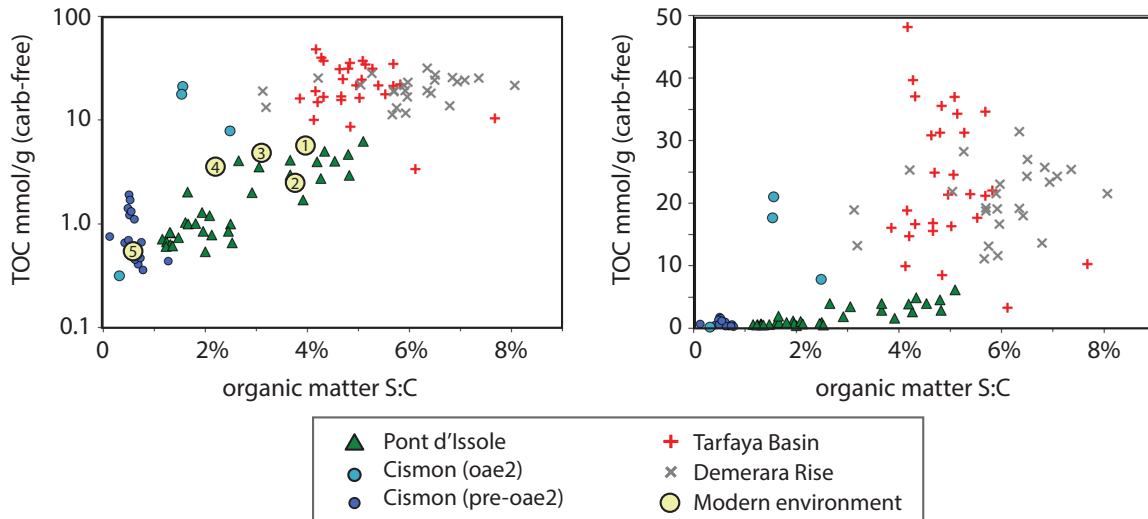
254 sulfides (Raven et al., 2018).

255

256 **Discussion**

257

258 **1. Organic S:C and local redox state**

259

Fig. 6 Global relationship between sulfurization intensity and TOC preservation.
Relationships between the intensity of sulfurization (molar S:C ratio) and TOC
concentrations (mmol/g on a carbonate-free basis) are shown on log (left) and linear
(right) scales; for versions of these plots on a whole-rock basis, see Supplementary Figure
1. Circled numbers on left panel refer to published values from modern environments: (1)
Cariaco Basin sediments (Werne et al., 2003); (2) the Peru Margin, (Eglinton et al.,
1994); (3) the Namibian Margin, (Dale et al., 2009); (4) Santa Barbara Basin sediments,
(Raven et al., 2016b); and (5) Gulf of Lion sediments (Supplementary Table 1).

Results from Cismon, Tarfaya Basin, and Demerara Rise extend the relationship between
OM S:C ratio and abundance that was seen in Pont d'Issole (Raven et al., 2018), with
samples ranging from OM–poor limestones to shales composed almost entirely of OM
and carbonate (Figure 6). In addition to providing an indicator of the relative intensity of
sulfurization reactions, the S:C ratio of OM can be used to infer the rate(s) and location
of sulfurization (e.g., in particles sinking through the water column, at the sediment-water
interface, or within the sediments). Elevated OM S:C ratios require organic substrates

277   with a high density of functional groups available to react with (poly)sulfide; we refer to

278   these groups as functionally 'sulfurizable moieties,' recognizing that certain moieties

279   may be conditionally sulfurizable, contingent on the chemical and physical properties of

280   the environment (Blair and Aller, 2012). Still, we broadly expect the highest

281   concentrations of sulfurizable moieties in surface water, where fresh marine OM is

282   relatively rich in sulfurizable aldehydes, alcohols, and conjugated double bonds (Amrani

283   and Aizenshtat, 2004). The concentration of these moieties in particulate OM will

284   decrease with depth as microbial heterotrophs degrade and consume oxygen- and energy-

285   rich components of the milieu like sugars and proteins (Hedges et al., 1999).

286

287   Figure 6 illustrates how the relationship between the S:C ratio and concentration of OM

288   for the four compiled OAE-2 sites compares with published data from modern

289   environments with different redox conditions. Bottom waters from Cariaco Basin

290   (labeled '1') are sulfidic below ~250 m water depth (Werne et al., 2003); bottom waters

291   from the Peru ('2') and Namibian ('3') Margins are O_2-depleted but rarely sulfidic, with

292   sulfidic sediments (Dale et al., 2009; Eglinton et al., 1994); bottom waters in Santa

293   Barbara Basin ('4') are intermittently oxic, with sulfidic sediments; and both the bottom

294   water and shallow sediments in the Gulf of Lion sediments ('5') are oxic. Among these

295   modern sites, S:C ratios and OM concentrations are highest in sediments from the sulfidic

296   Cariaco Basin and lowest in sediments from the oxic Gulf of Lion. Sites with varying

297   degrees of bottom water O_2 depletion fall in between these end members, overlapping

298   with Pont d'Issole shales that similarly imply a chemocline near the sediment-water

299   interface (Raven et al., 2018). Of course, each of these sites is also affected by unique

300   chemical and physical characteristics of the environment. For example, high

301   sedimentation rates are observed on the Peru Margin due to the weathering of the Andes,

302   which presumably dilutes TOC concentrations relative to sites with more moderate

303   sedimentation rates (Fig. 6). Despite this caveat, these modern sites conform to a trend

304   toward higher S:C ratios and higher OM concentrations associated with increasingly O_2-

305   limited environments.

306

307   The S:C ratios and TOC concentrations in modern sites overlap with the range of data

308   from Pont d'Issole and Cismon. At Pont d'Issole, variations in OM S:C ratio and OM

309   concentration correspond with changes in lithology and appear to record movement of the

310   chemocline between diffusively restricted sediments and the deeper water column (Raven

311   et al., 2018). In this interpretation, OM S:C ratios near 5% derive from rapid OM

312   sulfurization reactions in the water column or near the sediment-water interface, where

313   OM contains at least this concentration of functionally sulfurizable moieties, while during

314   more oxic periods, sulfurization in sediments affects older OM ($\geq$10s of years) with a

315   lower concentration of sulfurizable moieties and yields OM S:C ratios closer to 2%. The

316   redox speciation of OS from these purportedly oxic periods, as seen by XAS, is variable

317   and distinct from OS in strongly sulfurized materials. In contrast, the distribution of OS

318   redox states in strongly sulfurized OM is remarkably consistent within and among sites

319   (Fig. 5). XAS results thus indicate that lower S:C ratios in some Pont d'Issole samples do

320   not reflect simple dilution with a non-sulfurizable OM pool; instead, they indicate that

321   sulfurization reactions involved a different suite of sulfurizable organic precursors, a

322   different sulfur reactant (sulfide vs. polysulfide), or both.

323

324   Like at Pont d'Issole, OM-rich black shales from Cismon have previously been linked

325   with bottom water anoxia based on sedimentological and bulk geochemical observations

326   (Bellanca et al., 1996b). Cismon black shales have moderate S:C ratios (1.5–2.5%) but

327   relatively high TOC concentrations compared with the other sites in Fig. 6, a potential

328   effect of low sedimentation rates. On the other end of the spectrum, low-TOC limestones

329   from Cismon are rich in benthic foraminifera, indicating generally oxic deposition. These

330   sediments are comparable with low-TOC limestones from Pont d'Issole and modern oxic

331   sediments from the Gulf of Lion, with typical S:C ratios of ≤1% (Fig. 6).

332

333   Southern proto–North Atlantic OAE-2 samples extend the trend in Figure 6 toward even

334   greater OM concentrations and S:C ratios than those associated with bottom water anoxia

335   at Cismon, Pont d'Issole, and modern sites. We lack modern analogues for these

336   remarkable hotspots of organic C burial, which had an outsized role in driving changes in

337   the OAE-2 C and S cycles (Sinninghe Damsté et al., 1998; Kolonic et al., 2005). At both

338   Demerara Rise and Tarfaya Basin, there is abundant evidence for water column euxinia

339   and at least intermittant photic zone anoxia. Finely laminated sediments from Demerara

340   Rise (Erbacher et al., 2005) contain only occasional benthic foraminifera (Friedrich et al.,

341   2006), iron speciation documents local sulfidic conditions (Owens et al., 2016), and trace

342   metals also suggest reducing local conditions (Hetzel et al., 2009) that expand globally

343   during the event (Owens et al., 2016). At Tarfaya, an anoxic and commonly sulfidic

344   water column is evidenced by iron speciation, organic petrography, and the presence of

345   biomarkers for phototrophic sulfide oxidizing bacteria (in nearby core S13, (Kuypers et

346   al., 2002; Poulton et al., 2015). Still, there is also evidence for periodic, short–lived

347   intervals of less strongly reducing conditions (Poulton et al., 2015), potentially

348   contributing to slightly lower OM S:C ratios at this site than at Demerara. In general,

349   however, reducing conditions at both southern proto–North Atlantic sites could have

350   facilitated rapid, extensive sulfurization of a large pool of fresh OM in sinking particles

351   with a high concentration of functionally sulfurizable moieties (Sinninghe Damsté et al.,

352   1998). We emphasize that, in contrast with prior work, our conceptual model invokes

353   near–instantaneous reactions between OM with some concentration of sulfurizable

354   moieties and polysulfide, wherever sulfide and oxidants are first available in the

355   environment. Polysulfide 'availability' for sulfurization will depend on microbial sulfate

356   reduction rates, oxidant availability, and competition with Fe; importantly, however, it

357   does not necessarily imply measurable free sulfide in the ('bulk') water column.

358

359   We can also compare these OAE-2 data with the results of laboratory experiments

360   utilizing algal biomass or model compounds. In the presence of excess polysulfides,

361   lipids and carbohydrates sulfurize to form macromolecular material in which

362   characteristic components have S:C ratios around 2–3% (Gelin et al., 1998) and ~6.7%

363   (van Dongen et al., 2003), respectively. For dissolved organic matter, bulk molar S:C

364   ratios can apparently be much higher, reaching as much as 15% in recent experiments

365   (Pohlabeln et al., 2017). Still, the average S:C ratios of (bulk, particulate) OM from

366   Tarfaya (5.0%), Demerara (5.9%), and Cismon shales (5.0%) indicate that the OM

367   sulfurizing in these environments had a concentration of sulfurizable moieties similar to

368   the constituents of fresh, carbohydrate–rich algal biomass. Experimental data thus lend

369   credence to the hypothesis that rapid, likely particle-hosted, sulfurization drove OM

370   preservation in the water columns of both Tarfaya Basin and Demerara Rise.

371

372   The relationship between S:C ratio, OM preservation, and local redox structure therefore

373   appears to be generalizable for marine environments, albeit with the important caveat that

374   concentration data are affected by local sedimentation rate. The observation that OM

375   sulfurization is an apparently major control on OM burial in diverse redox settings invites

376   parameterization and application of this trend to models of carbon cycling on local to

377   global scales and throughout the geologic record.

378

379

380   **2. Interpreting organic matter and pyrite δ^{34}S records**

381

382   To first order, the sulfur isotope compositions of pyrite and organic S reflect the δ^{34}S

383   value of sulfide and/or polysulfide in the environment where that solid phase formed,

384   with OM commonly ~5–10‰ more ^{34}S-enriched than coexisting pyrite (Anderson and

385   Pratt, 1995). Accordingly, S–isotope ratios – of both pyrite and OM – provide potentially

386   powerful archives of information about the availability and distribution of sulfide in the

387   environment. Several primary factors affect the integrated (poly)sulfide δ^{34}S recorded in

388   pyrite and OM, including (1) the δ^{34}S value of the sulfate used in microbial sulfate

389   reduction (MSR; (Fike and Grotzinger, 2008); (2) the fractionation factor associated with

390   MSR (ε_{MSR}, (Kaplan and Rittenberg, 1964)); (3) the position of the chemocline relative to

391   diffusively 'closed' sediments (Jorgensen, 1979) and (4) the concentration of sulfate and

392   resulting depth of sulfate depletion (Adams et al., 2010). Importantly, all of these

393   processes impact the distribution and/or $\delta^{34}S$ value of (poly)sulfide in the environment

394   and should therefore impact the S-isotope composition of both pyrite and OM, generating

395   roughly parallel $\delta^{34}S$ profiles. If pyrite and OM $\delta^{34}S$ profiles are not parallel, then we

396   need to invoke processes that affect these sinks differently.

397
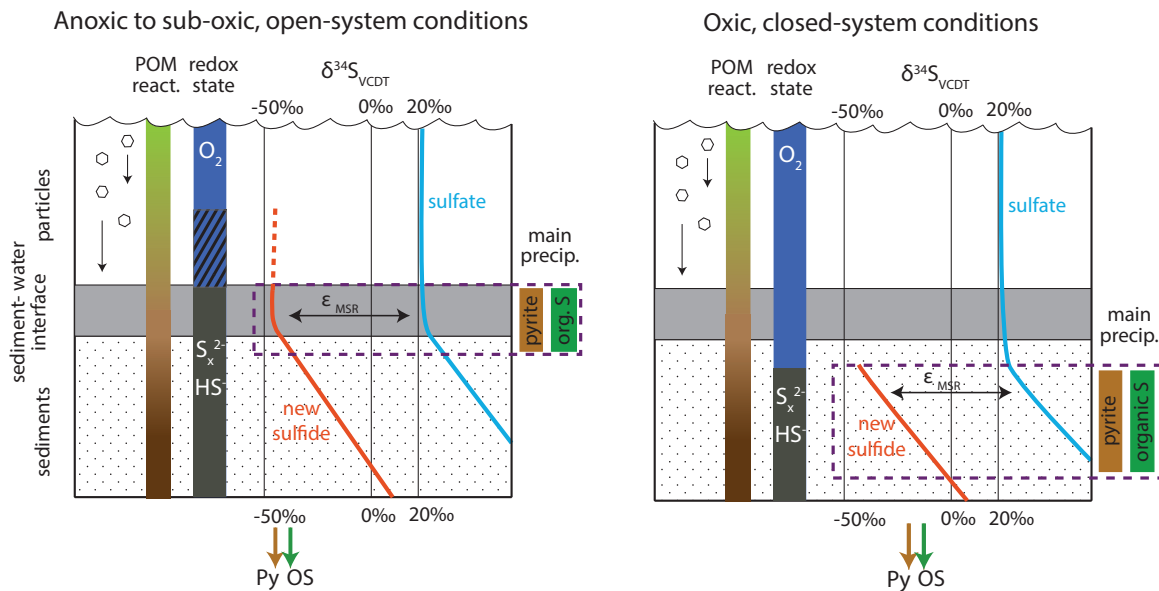
398

399   **Fig. 7: Model for organic S and pyrite formation at Pont d'Issole and Cismon.** The

400   color scale labeled "POM react." represents a generalized decline in the reactivity of

401   particulate OM with age since export from the photic zone. At left, the dashed red line

402   and hatched redox state depict differences between sub-oxic and anoxic conditions.

403   Under anoxic conditions, the zone of precipitation for pyrite and organic S would move

404   upward with the chemocline. Diagram is not to scale.

405

406   At Pont d'Issole, OM and pyrite $\delta^{34}S$ profiles move in near–parallel between the TOC-

407   rich and TOC-lean layers associated with OAE-2 (Fig. 2). In a previous study, we

408   attributed these $\delta^{34}S$ trends in OM to changes in the position of the chemocline in the

409   paleo-environment, meaning that MSR moved between environments that were

410   diffusively open or closed systems with respect to sulfate, shown schematically in Fig. 7.

411   Under conditions where O_2 concentrations are drawn down to zero at roughly the

412   sediment-water interface (which we call 'sub-oxic' in Fig. 7), MSR in the shallowest

413   sediments can access the open-ocean pool of seawater sulfate with an unfractionated $\delta^{34}S$

414   value, and the resulting strongly ^{34}S-depleted sulfide from MSR is recorded in both pyrite

415   and OM. Under more 'oxic' conditions, O_2 penetrates deeper in the sediments and

416   microbial sulfate reduction occurs in a diffusively sulfate–limited environment. As

417   available sulfate is consumed with some fractionation (ε_{MSR}), residual sulfate in

418   porewater becomes enriched in ^{34}S, and the organic and inorganic sulfur pools that

419   precipitate within such a (partially) closed system have higher integrated $\delta^{34}S$ values than

420   those formed in open systems. At Pont d'Issole, S–isotope evidence for closed-system

421   MSR is also associated with smaller amounts of preserved OM with a lower S:C ratio.

422

423   The S-isotope data for OS and pyrite from Cismon shales are consistent with the open–

424   vs–closed system dynamics indicated at Pont d'Issole. Both phases are strongly ^{34}S-

425   depleted during the OAE C-isotope excursion, indicating generally open-system pyrite

426   and OS formation. These low $\delta^{34}S$ values are similar to S-isotope data observed in

427   sediments from modern sulfidic basins, which have been attributed to open-system

428   formation (Lyons et al., 2003). As noted by the dashed vertical red line in Fig. 7, the

429   critical sulfidic environment(s) hosting these reactions could be very shallow sediments

430   and/or particles sinking through the water column.

431

432
433
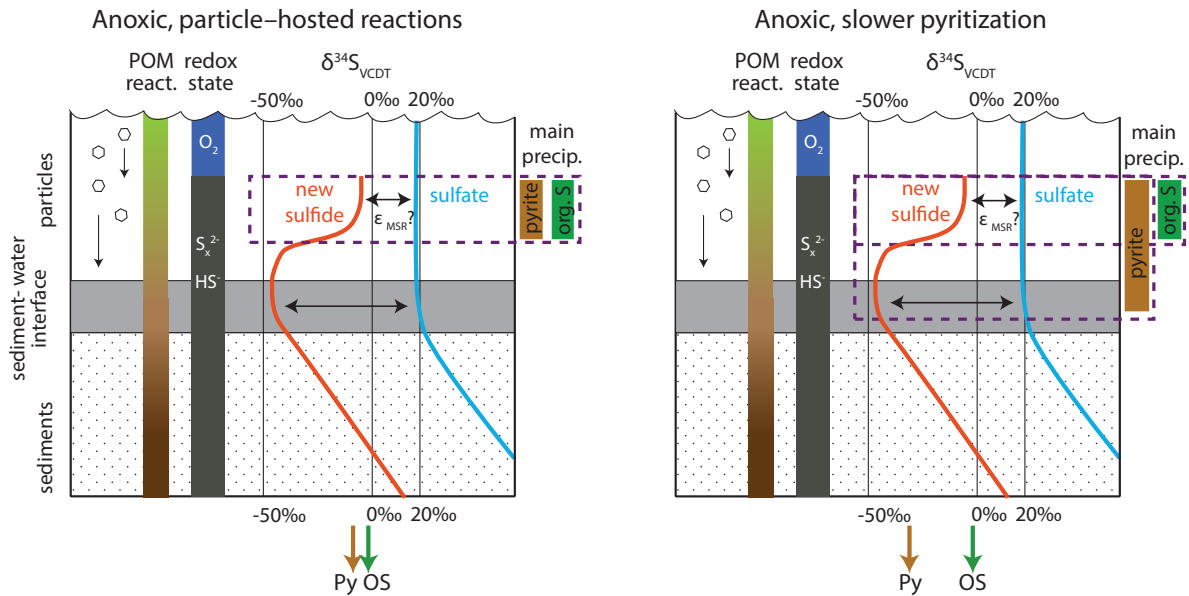
Fig. 8 Proposed model for OAE-2 δ^{34}S records at Tarfaya and Demerara. Left panel

shows hypothesized conditions $\geq$190,000 yrs before the onset of OAE-2. Right panel

shows a scenario for explaining pyrite and OM δ^{34}S values during the early part of the

OAE-2 C-isotope excursion. The color scale labeled "POM react." represents a

generalized decline in the reactivity of particulate OM with age since export from the

photic zone. Diagram is not to scale.

440

In contrast, different processes impact δ^{34}S patterns at Tarfaya Basin and Demerara Rise.

A wealth of data supports the idea that the Tarfaya Basin and Demerara Rise water

columns were typically euxinic before and after OAE-2, which would imply open-system

S cycling that leads to ^{34}S-depleted pyrite and OM. Yet, δ^{34}S values of pyrite and OM

from both of these sites are near –5‰ at these times, much more ^{34}S-enriched than

samples from other sites with open-system MSR. To reconcile these observations, we

23

447 propose that the δ^{34}S values recorded in plentiful OM at Tarfaya Basin and Demerara

448 Rise do reflect the S-isotope composition of sulfide in sinking particles, and that this

449 sulfide was relatively ^{34}S-enriched (Fig. 8). Similarly, there is limited evidence for the

450 existence of transiently ^{34}S-enriched sulfide in particles from Cariaco Basin, despite deep

451 basin sulfide δ^{34}S values that are consistently near –30‰ (Li et al., 2010). During a

452 period of peak productivity and apparent sulfurization, the elemental S in sinking

453 particles had δ^{34}S values between –5.9 and 18.9‰ (Raven et al., 2016a), a δ^{34}S offset

454 from seawater sulfate of only 2 to 27‰. The dramatic enrichment inferred for particle

455 sulfide δ^{34}S values at Tarfaya Basin and Demerara Rise (Fig. 8) contrasts with the slight

456 (~5‰) enrichments frequently observed in the uppermost portion of modern sulfidic

457 water columns (Lyons et al., 2003), which are attributed to oxidative S-cycling

458 microorganisms and/or abiotic sulfide oxidation. Thus, the ^{34}S-enriched patterns in OM

459 and pyrite in OM-rich sediments may capture the signature of MSR occurring rapidly in

460 sinking particles.

461

462 The large fluxes of fresh OM that reached O_2-limited parts of the environment in both

463 Tarfaya Basin and Demerara Rise make these sites likely candidates for the operation of

464 rapid, substrate-replete MSR, which could lead to relatively ^{34}S-enriched sulfide in

465 particles via smaller fractionations during sulfate reduction, sulfate drawdown within

466 diffusively limited microenvironments, or both. The fractionation factor associated with

467 MSR (ε_{MSR}) is highly variable and depends broadly on the rate of MSR (Kaplan and

468 Rittenberg, 1964). Although most marine systems have apparent fractionation factors

469 closer to the equilibrium fractionation between sulfate and sulfide of 72‰, low ε_{MSR}

470   values (<25‰) are associated with high rates of cell-specific MSR, on the order of >25

471   fmol H_2S/cell/day (Wenk et al., 2017), observed for sulfate reducers in laboratory settings

472   with plentiful carbon substrates and nutrients. These "small" S-isotope fractionations are

473   consistent with the 20–30‰ difference between seawater sulfate (at ~19‰) and apparent

474   particle-hosted sulfide observed at Tarfaya Basin and Demerara Rise. Alternatively or in

475   addition to changes in ε_{MSR}, if particles are sufficiently large (>> 1 mm), it is possible for

476   sulfate to become diffusively limited within particle microenvironments (Louca and

477   Crowe, 2017). Very high rates of MSR could therefore drive the remaining sulfate pool

478   within microenvironments toward higher $\delta^{34}S$ values and contribute to relatively ^{34}S-

479   enriched sulfide.

480

481   The alternative explanation for our results attributes the relatively ^{34}S-enriched

482   composition of pyrite and OM at Tarfaya and Demerara prior to the onset of the OAE to

483   their formation from sediment porewater. Importantly, it also requires that these phases

484   form semi-continuously during burial to the depths at which sulfate is nearly fully drawn

485   down, in order to integrate to bulk compositions near –5‰. Barring extreme

486   sedimentation events, this implies maximum OM sulfurization rates on the timescales of

487   at least tens to hundreds of years – sufficient to accumulate a diffusively limiting layer –

488   not the days to weeks observed in Cariaco particles and laboratory experiments.

489   Additionally, this explanation for Tarfaya and Demerara $\delta^{34}S$ patterns is difficult to

490   reconcile with the S:C ratio of OM. For OM to incorporate up to 6 mol% S gradually

491   over at least years of aging, that OM must have retained a high density of sulfurizable

492   moieties that were somehow also effectively inaccessible to heterotrophs. Theoretically,

493   this could result from enhanced preservation mechanisms other than sulfurization,

494   notably physical protection by association with clays or other mineral surfaces (Hedges

495   and Keil, 1995). Still, the sheer abundance of OM in Tarfaya and Demerara sediments

496   would overwhelm available clays, and it is difficult to envision a mechanism to sulfurize

497   OM after many years of effective physical protection. We therefore consider a purely

498   closed-system sedimentary origin for the moderately ^{34}S-enriched OM and pyrite at

499   Tarfaya and Demerara improbable.

500

501   Similar to OM throughout the section, pyrite in the lowest part of the section at both

502   Tarfaya Basin and Demerara Rise has relatively high δ^{34}S values. Under these pre-OAE-

503   2 conditions, the offset between pyrite and OM δ^{34}S values is only 5–10‰, similar to the

504   offset observed in other environments that are thought to host open-system concurrent

505   pyritization and OM sulfurization (Cariaco Basin, Cismon). Starting significantly before

506   the onset of OAE-2, pyrite δ^{34}S begins to move independently of OM δ^{34}S, increasing

507   $\Delta\delta^{34}S_{OS-py}$ values. Little-to-no concurrent shift is seen in the OM δ^{34}S record, and OM

508   has a consistent S redox composition (as assessed by XAS, Fig. 5) throughout the section.

509   Therefore, the shift in pyrite δ^{34}S values is not the result of changing sulfide distribution

510   or ε_{MSR} in the environment. Instead, this independent variability is caused by a process

511   that impacts the kinetics of one sulfide sink relative to the other. In the case of pyrite at

512   the onset of OAE-2 at Tarfaya and Demerara Rise, the observed shift indicates that the

513   zone of pyrite formation expanded into deeper portions of the water column and/or

514   sediment, integrating more ^{34}S-depleted sulfide generated from MSR at more typical

515   (slow) environmental rates (Fig. 8).

516

3. Global pyrite δ^{34}S patterns and OAE-2 implications

518

519
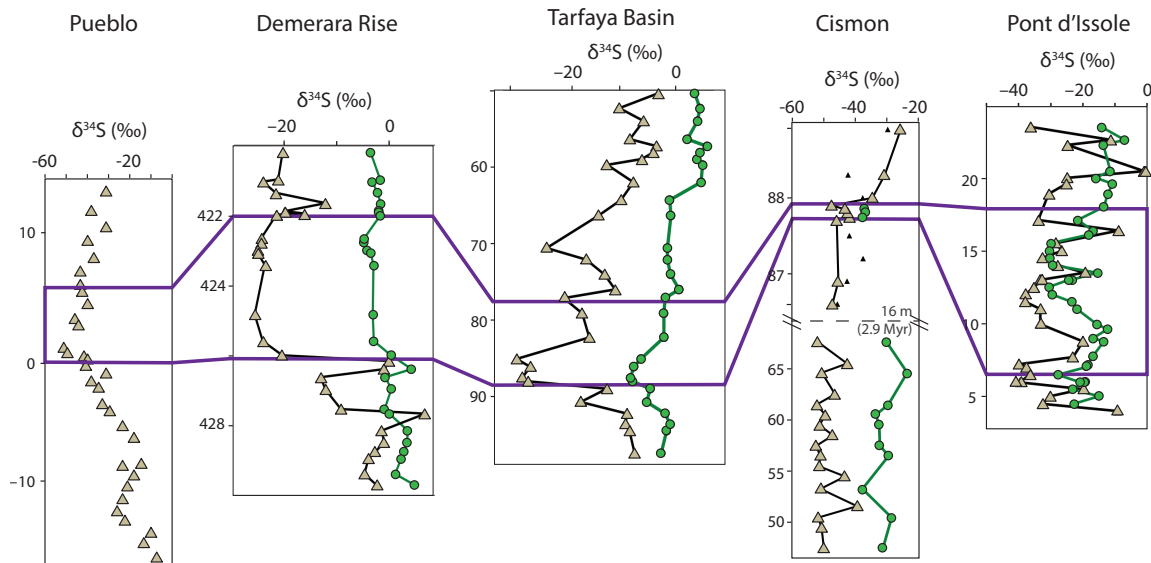
Fig. 9 Summary of δ^{34}S records across OAE-2. Green circles show OM δ^{34}S values

and brown triangles show pyrite δ^{34}S values. Pueblo data is from (Adams et al., 2010).

The gap in the Cismon y-axis represents 16 m of OM-lean carbonates (~2.9 Myr), and

small black triangles are previously published data from (Gomes et al., 2016). The C-

isotope excursion, representing an estimated 500 kyr of accumulation, is outlined in

purple. Pyrites from Demerara Rise, Tarfaya Basin, and Pueblo all become more ^{34}S-

depleted leading up to the onset of OAE-2.

527

The decrease in pyrite δ^{34}S values prior to the onset of OAE-2 appears to be a widespread

phenomenon, with remarkably similar profiles from Demerara Rise, Tarfaya Basin, and

the Western Interior Seaway (Pueblo (Adams et al., 2010), Fig. 9). Because the ~20‰

negative δ^{34}S shift in pyrite at Tarfaya and Demerara is not observed in the δ^{34}S profile of

532   OM, it is not likely to primarily reflect changes in the spatial distribution or $\delta^{34}S$ of

533   dissolved sulfide in the environment. Instead, we propose that pyrite $\delta^{34}S$ patterns record

534   changes in marine iron cycling across OAE-2, which impacted the kinetics of pyrite

535   precipitation and extended the zone of pyrite precipitation deeper in the sedimentary

536   profile.

537

538   The iron available for pyritization in marine environments is sourced from a mixture of

539   detrital iron from the continents, hydrothermal iron from spreading ridges, and

540   remobilized iron from biogeochemical cycling in shelf sediments. Most sediments from

541   the southern proto–North Atlantic during OAE-2 have elevated Fe_T/Al ratios (>0.5, the

542   crustal average value) and near–zero $\delta^{56}Fe$ compositions, suggesting that a significant

543   component of the iron delivered to these sites was from hydrothermal sources (Owens et

544   al., 2012). The processes that facilitate the transport of hydrothermally-sourced iron

545   remain subjects of active research, but appear to involve stabilization of Fe^{3+} in colloidal

546   or nanoparticulate phases (Fitzsimmons et al., 2017). Hydrothermal iron that encounters

547   dissolved sulfide can precipitate as an Fe-sulfide and be trapped in place as pyrite,

548   restricting the amount of iron that can be transported through euxinic basins to distal

549   sites. In contrast, iron is highly mobile in anoxic but non-sulfidic seawater. The delivery

550   of iron to Demerara Rise and Tarfaya Basin was therefore likely sensitive to the redox

551   state of nearby environments, and hydrothermal iron delivery could have been

552   significantly curtailed by nearby euxinia.

553

554 In addition to impacting the total flux of iron transported throughout the basin, expanding

555 anoxia is likely to affect its mineralogy. The source of Fe for pyritization is commonly

556 presumed to be dissolved Fe^{2+}, which can be released from Fe^{III}-bearing minerals by

557 reduction either abiotically with bisulfide (Canfield, 1989) or biotically by Fe-reducing

558 microorganisms. The rates of both types of iron reduction vary depending on the

559 mineralogy and specific surface area of the Fe^{III} involved: poorly crystalline

560 oxyhydroxides like ferrihydrite and lepidocrocite are reduced within hours to days, while

561 crystalline oxides and oxyhydroxides like goethite and hematite are reduced more slowly,

562 and Fe-bearing silicates can persist for millennia (Raiswell et al., 2018). Where

563 concentrations of Fe^{2+} and sulfide in solution are sufficiently high, pyrite precipitation is

564 generally thought to proceed via precipitation of an iron monosulfide intermediate that

565 subsequently converts to pyrite. Intriguingly, (Wan et al., 2017) recently described a

566 second category of pyritization mechanism with the potential to drive pyrite formation

567 where Fe^{III}–oxide surfaces are plentiful and vastly exceed the available HS^-. Under these

568 conditions, ferric hydroxide surfaces can mediate the rapid nucleation of pyrite via the

569 formation of $>Fe^{II}S_2^-$, making redox interfaces and sinking particles with high Fe^{III}:HS^-

570 ratios potential hotspots for surface-mediated pyritization of ferric hydroxides. Ferric

571 hydroxides from any source (hydrothermal, detrital, or remobilized) would have been less

572 likely to reach already-euxinic sites like Demerara Rise and Tarfaya Basin as regional

573 euxinia expanded, raising the possibility that the negative shift in pyrite S-isotopes

574 reflects a reduction in the significance of this pyritization mechanism. Changing regional

575 redox could also impact the mineralogy of remobilized Fe more broadly by changing the

576 rates and/or environmental conditions of (oxy)hydroxide formation during repetitive

577 redox cycling, generating a different suite of Fe^{III} minerals that re-release Fe^{2+} into the

578 depositional environment at diverse rates. The bulk pyrite $\delta^{34}S$ records we present here

579 reflect the integrated pool of pyrite derived from precipitation on multiple timescales of

580 Fe^{III}–mineral (re-)reduction as well as potentially from ferric hydroxide surface–mediated

581 reactions. Separating these various contributors to bulk pyrite records will be essential to

582 understand how expanding regional anoxia and euxinia impacted the abundance and

583 mineralogy of iron sources and, by extension, the kinetics of pyritization.

584

585 Trace metal concentrations and thallium isotopes from Demerara Rise provide evidence

586 for the expansion of regional to more global anoxia prior to the onset of the OAE-2 C-

587 isotope excursion (Ostrander et al., 2017; Owens et al., 2016). Like iron, the redox-

588 sensitive elements Zn, V, and Mo are readily sequestered in anoxic and/or sulfidic

589 sediments, and this process is thought to be responsible for their apparent removal from

590 seawater prior to OAE-2 (Owens et al., 2016). Using an extrapolation of the estimated

591 OAE-2 linear sedimentation rate (0.8 cm/kyr) to 427.5 m, pyrite $\delta^{34}S$ values at Demerara

592 begin to decrease ~190 kyr before the onset of OAE-2. This depth corresponds to the

593 initial drop in concentrations of Zn in this core, a sensitive indicator of anoxic conditions

594 with a short residence time (~11 kyr, (Little et al., 2014)). The decrease in pyrite $\delta^{34}S$

595 values culminates at the onset of the OAE, in sediments evidencing drawdown of even

596 sulfide-sensitive Mo, indicating prevalent sulfidic environments (Owens et al., 2016).

597 The gradual pre-OAE pyrite $\delta^{34}S$ shift at Demerara thus corresponds to a period of

598 intensification of regional to global anoxia prior to the OAE and an expansion of sulfidic

599 conditions globally (Owens et al., 2013).

600

601   Changes in the delivery of iron to sites in the southern proto–North Atlantic could have

602   generated the shift in pyrite $\delta^{34}S$ that we observe by slowing the kinetics of pyrite

603   formation. For example, if the combination of expanding euxinia and volcanic activity

604   caused the main source of Fe at these sites to switch from more hydrothermally sourced,

605   organic–complexed Fe^{III} to detrital or volcanic crystalline oxy-hydroxides, the rate of

606   Fe^{2+} release to solution in sinking marine particles could have dropped dramatically. The

607   conceptual model put forth in Fig. 7 predicts that this scenario would yield more ^{34}S-

608   depleted pyrite overall. Importantly, this could occur while the total quantity of pyrite

609   eventually buried remained nearly constant.

610

611   At Pueblo and Tarfaya Basin, the onset of the shift toward more ^{34}S-depleted pyrite is

612   staggered relative to Demerara Rise (Fig. 9). Using published interpolated Ar-Ar ages

613   from ammonite biozones, pyrite $\delta^{34}S$ values at Pueblo drop in two stages at ~400 kyr and

614   ~200 kyr before the onset of OAE-2 (Adams et al., 2010). At Tarfaya Basin, if we

615   extrapolate estimated OAE-2 accumulation rates (3.3 cm/kyr) similar to Demerara, then

616   the pyrite $\delta^{34}S$ shift occurs ~82 kyr before the OAE. Osmium, strontium, and other

617   geochemical proxies indicate regional heterogeneity in hydrothermal activity in different

618   ocean basins at this time (du Vivier et al., 2014), which would also impact hydrothermal

619   iron fluxes (Owens et al., 2012). Importantly, the Western Interior Seaway has a different

620   redox structure leading up to OAE-2 than the rest of the proto-North Atlantic and Tethys,

621   which likely leads to differences in the history of iron cycling among these sites.

622

623   Records from OAE-2 exemplify how the timing and location of pyritization can be

624   affected by changes in iron biogeochemistry in addition to changes in sulfur cycling.

625   They also suggest that organic S should be incorporated into future models for the S

626   cycle for OAEs. For example, because organic S is more typically more [34]S-enriched than

627   pyrite, previous estimates for the extent of euxinia during OAE-2 based on S-isotope

628   mass balance (e.g., Owens et al., 2013) may be conservative. OM sulfurization could

629   have been important factor for driving high organic carbon mass accumulation rates even

630   for localities with low total organic carbon (Owens et al., 2018), supporting massive

631   global OC burial. By investigating the S-isotope behavior of both pyrite and OM, we can

632   begin to take full advantage of these complex and powerful archives.

633

634   **Conclusions**

635   In sedimentary sections spanning OAE-2, the S-isotope compositions of pyrite were

636   impacted by the confluence of local redox structure, the fractionation associated with

637   microbial sulfate reduction (ε_{MSR}), and the speciation of Fe in the environment, while the

638   S-isotope compositions of OM appear to predominantly reflect changes in local redox

639   structure and/or ε_{MSR}. Accordingly, paired OM and pyrite $\delta^{34}S$ profiles make it possible

640   to disentangle the effects of chemocline position, sulfate reduction rate, and regional-to-

641   global geochemical perturbations on S-isotopes in the rock record.

642

643   Particle-hosted OM sulfurization may be a primary control on OM preservation during

644   periods of widespread OM burial. Explicit consideration of rapid OM sulfurization in O_2-

645   limited environments thus has the potential to improve models of organic C preservation

646   and remineralization in both modern and ancient systems. Additionally, in the several

647   hundred thousand years leading up to the onset of OAE-2, paired pyrite and OM δ^{34}S

648   records indicate a globally widespread change in the timing of pyrite formation relative to

649   OM sulfurization. The regional expansion of euxinic conditions and changes in volcanic

650   activity may have contributed to changes in the speciation of iron available for

651   pyritization and thus to the relatively slow formation of relatively ^{34}S-depleted pyrite

652   during the OAE. This change in global Fe-cycling could not be identified from pyrite

653   δ^{34}S profiles alone, underscoring the value and untapped potential of paired pyrite – OM

654   S-isotope records for exploring geologic archives.

655

656

669

Supplemental Information:

671   Fig. S1: whole-rock basis version of Fig. 6

672   Table S1: Gulf of Lion average composition

673   Table S2: Compiled geochemical results

674   Table S3: Compiled XAS results

675

676 **References**

677 Adams, D.D., Hurtgen, M.T., Sageman, B.B., 2010. Volcanic triggering of a
678   biogeochemical cascade during Oceanic Anoxic Event 2 3, 201–204.

679 Amrani, A., Aizenshtat, Z., 2004. Mechanisms of sulfur introduction chemically
680   controlled: δ34S imprint. Organic Geochemistry 35, 1319–1336.
681   doi:10.1016/j.orggeochem.2004.06.019

682 Anderson, T.F., Pratt, L.M., 1995. Isotopic evidence for the origin of organic sulfur and
683   elemental sulfur in marine sediments 612, 378–396.

684 Bellanca, A., Claps, M., Erba, E., Masetti, D., Neri, R., 1996a. Orbitally induced
685   limestone/marlstone rhythms in the Albian—Cenomanian Cismon section (Venetian
686   region, northern Italy): Sedimentology, calcareous and siliceous …. Palaeogeography
687   126, 227–260. doi:10.1016/S0031-0182(96)00041-7

688 Bellanca, A., Claps, M., Erba, E., Masetti, D., Neri, R., Premoli Silva, I., Venezia, F.,
689   1996b. Orbitally induced limestone/marlstone rhythms in the Albian—Cenomanian
690   Cismon section (Venetian region, northern Italy): Sedimentology, calcareous and
691   siliceous plankton distribution, elemental and isotope geochemistry.
692   Palaeogeography, Palaeoclimatology, Palaeoecology 126, 227–260.
693   doi:10.1016/S0031-0182(96)00041-7

694 Blair, N.E., Aller, R.C., 2012. The Fate of Terrestrial Organic Carbon in the Marine
695   Environment. Annu. Rev. Mar. Sci. 4, 401–423. doi:10.1146/annurev-marine-
696   120709-142717

697 Boussafir, M., Gelin, F., Lallier-Verges, E., Derenne, S., Bertrand, P., Largeau, C., 1995.
698   Electron microscopy and pyrolysis of kerogens from the Kimmeridge Clay
699   Formation, UK: Source organisms, preservation processes, and origin of microcycles.
700   Geochimica et Cosmochimica Acta 59, 3731–3747.

701 Canfield, D.E., 1989. Reactive iron in marine sediments. Chemical Geology 53, 619–632.
702   doi:10.1016/0016-7037(89)90005-7

703 Canfield, D.E., Raiswell, R., Westrich, J.T., Reaves, C.M., 1986. The use of chromium
704   reduction in the analysis of reduced inorganic sulfur in sediments and shales.
705   Chemical Geology.

706 Dale, A.W., Bruchert, V., Alperin, M., Regnier, P., 2009. An integrated sulfur isotope
707   model for Namibian shelf sediments. Geochimica et Cosmochimica Acta 73, 1924–
708   1944. doi:10.1016/j.gca.2008.12.015

709 Damsté, J., Letters, J.K.E.A.P.S., 1998, 1998. A euxinic southern North Atlantic Ocean
710   during the Cenomanian/Turonian oceanic anoxic event. Chemical Geology 158, 165–
711   173.

712 Eglinton, T.I., Irvine, J.E., Vairavamurth, Zhou, W., Manowitz, B., 1994. Formation and
713   diagenesis of macromolecular organic sulfur in Peru margin sediments. Organic
714   Geochemistry 22, 781–799.

715 Erbacher, J., Friedrich, O., Wilson, P.A., Birch, H., Mutterlose, J., 2005. Stable organic

716   carbon isotope stratigraphy across Oceanic Anoxic Event 2 of Demerara Rise,
717   western tropical Atlantic. Geochemistry Geophysics Geosystems 6, 714–9.
718   doi:10.1029/2004GC000850

719   Fike, D.A., Grotzinger, J.P., 2008. A paired sulfate–pyrite $\delta^{34}S$ approach to
720   understanding the evolution of the Ediacaran–Cambrian sulfur cycle. Geochimica et
721   Cosmochimica Acta 72, 2636–2648. doi:10.1016/j.gca.2008.03.021

722   Fitzsimmons, J.N., John, S.G., Marsay, C.M., Hoffman, C.L., Nicholas, S.L., Toner,
723   B.M., German, C.R., Sherrell, R.M., 2017. Iron persistence in a distal hydrothermal
724   plume supported by dissolved–particulate exchange. Nature Geosci 10, 195–201.
725   doi:10.1038/ngeo2900

726   Gambacorta, G., Jenkyns, H.C., Russo, F., Tsikos, H., Wilson, P.A., Faucher, G., Erba,
727   E., 2015. Carbon- and oxygen-isotope records of mid-Cretaceous Tethyan pelagic
728   sequences from the Umbria – Marche and Belluno Basins (Italy). Newsl. Stratigr. 48,
729   299–323. doi:10.1127/nos/2015/0066

730   Gelin, F., Kok, M.D., De Leeuw, J.W., Damsté, J.S.S., 1998. Laboratory sulfurisation of
731   the marine microalga Nannochloropsis salina. Organic Geochemistry 29, 1837–1848.

732   Gomes, M.L., Hurtgen, M.T., Sageman, B.B., 2016. Biogeochemical sulfur cycling
733   during Cretaceous oceanic anoxic events: A comparison of OAE1a and OAE2.
734   Paleoceanography 1–19. doi:10.1002/(ISSN)1944-9186

735   Hedges, J.I., Hu, F.S., Devol, A.H., Hartnett, H.E., Tsamakis, E., Keil, R.G., 1999.
736   Sedimentary organic matter preservation; a test for selective degradation under oxic
737   conditions. American Journal of Science 299, 529–555.

738   Hetzel, A., Böttcher, M.E., Wortmann, U.G., Brumsack, H.-J., 2009. Paleo-redox
739   conditions during OAE 2 reflected in Demerara Rise sediment geochemistry (ODP
740   Leg 207). Palaeogeography, Palaeoclimatology, Palaeoecology 273, 302–328.
741   doi:10.1016/j.palaeo.2008.11.005

742   Jarvis, I., Lignum, J.S., Gröcke, D.R., Jenkyns, H.C., 2011. Black shale deposition,
743   atmospheric CO2 drawdown, and cooling during the Cenomanian   Turonian Oceanic
744   Anoxic Event. Paleoceanography 26. doi:10.1029/2010PA002081

745   Jorgensen, B.B., 1979. A theoretical model of the stable sulfur isotope distribution in
746   marine sediments. Geochimica et Cosmochimica Acta 43, 363–374.

747   Kaplan, I.R., Rittenberg, S.C., 1964. Microbiological fractionation of sulphur isotopes.
748   Journal of General Microbiology 34, 195–212.

749   Keller, G., Adatte, T., Berner, Z., Chellai, E.H., Stueben, D., 2008. Oceanic events and
750   biotic effects of the Cenomanian-Turonian anoxic event, Tarfaya Basin, Morocco.
751   Cretaceous Research 29, 976–994. doi:10.1016/j.cretres.2008.05.020

752   Kolonic, S., Damsté, J., Böttcher, M.E., Kuypers, M.M.M., Kuhnt, W., Scheeder, G.,
753   Wagner, T., beckmann, B., 2002. Geochemical characterization of
754   Cenomanian/Turonian black shales from the Tarfaya Basin (SW Morocco). Journal
755   of Petroleum Geology 25, 325–350.

756   Kolonic, S., Wagner, T., Forster, A., Sinninghe Damsté, J.S., Walsworth-Bell, B., Erba,

757   E., Turgeon, S., Brumsack, H.-J., Chellai, E.H., Tsikos, H., Kuhnt, W., Kuypers,
758   M.M.M., 2005. Black shale deposition on the northwest African Shelf during the
759   Cenomanian/Turonian oceanic anoxic event: Climate coupling and global organic
760   carbon burial. Paleoceanography 20, n/a–n/a. doi:10.1029/2003PA000950

761   Kuypers, M.M.M., Pancost, R.D., Nijenhuis, I.A., Sinninghe Damsté, J.S., 2002.
762   Enhanced productivity led to increased organic carbon burial in the euxinic North
763   Atlantic basin during the late Cenomanian oceanic anoxic event. Paleoceanography
764   17, 3–1–3–13. doi:10.1029/2000PA000569

765   Li, X., Gilhooly, W.P., III, Zerkle, A.L., Lyons, T.W., Farquhar, J., Werne, J.P., Varela,
766   R., Scranton, M.I., 2010. Stable sulfur isotopes in the water column of the Cariaco
767   Basin. Geochimica et Cosmochimica Acta 74, 6764–6778.
768   doi:10.1016/j.gca.2010.08.020

769   Little, S.H., Vance, D., Walker-Brown, C., Landing, W.M., 2014. The oceanic mass
770   balance of copper and zinc isotopes, investigated by analysis of their inputs, and
771   outputs to ferromanganese oxide sediments. Geochimica et Cosmochimica Acta 125,
772   673–693. doi:10.1016/j.gca.2013.07.046

773   Louca, S., Crowe, S.A., 2017. Microscale reservoir effects on microbial sulfur isotope
774   fractionation. Geochimica et Cosmochimica Acta 203, 117–139.
775   doi:10.1016/j.gca.2017.01.007

776   Lyons, T.W., Werne, J.P., Hollander, D.J., Murray, R.W., 2003. Contrasting sulfur
777   geochemistry and Fe/Al and Mo/Al ratios across the last oxic-to-anoxic transition in
778   the Cariaco Basin, Venezuela. Chemical Geology 195, 131–157. doi:10.1016/S0009-
779   2541(02)00392-3

780   Ostrander, C.M., Owens, J.D., Nielsen, S.G., 2017. Constraining the rate of oceanic
781   deoxygenation leading up to a Cretaceous Oceanic Anoxic Event (OAE-2: ~94 Ma).
782   Science Advances 1–6.

783   Owens, J.D., Gill, B.C., Jenkyns, H.C., 2013. Sulfur isotopes track the global extent and
784   dynamics of euxinia during Cretaceous Oceanic Anoxic Event 2, in:. Presented at the
785   Proceedings of the …. doi:10.1073/pnas.1305304110/-/DCSupplemental

786   Owens, J.D., Lyons, T.W., Li, X., Macleod, K.G., 2012. Iron isotope and trace metal
787   records of iron cycling in the proto North Atlantic during the Cenomanian Turonian
788   oceanic anoxic event (OAE 2). Paleoceanography. doi:10.1029/2012PA002328

789   Owens, J.D., Lyons, T.W., Lowery, C.M., 2018. Quantifying the missing sink for global
790   organic carbon burial during a Cretaceous oceanic anoxic event. Earth and Planetary
791   Science Letters 499, 83–94. doi:10.1016/j.epsl.2018.07.021

792   Owens, J.D., Reinhard, C.T., Rohrssen, M., Love, G.D., Lyons, T.W., 2016. Empirical
793   links between trace metal cycling and marine microbial ecology during a large
794   perturbation to Earth's carbon cycle. Earth and Planetary Science Letters 449, 407–
795   417. doi:10.1016/j.epsl.2016.05.046

796   Pohlabeln, A.M., Gomez-Saez, G.V., Noriega-Ortega, B.E., Dittmar, T., 2017.
797   Experimental Evidence for Abiotic Sulfurization of Marine Dissolved Organic
798   Matter. Front. Mar. Sci. 4, 265. doi:10.3389/fmars.2017.00364

799   Poulton, S.W., Henkel, S., März, C., Urquhart, H., Flögel, S., Kasten, S., Sinninghe
800   Damsté, J.S., Wagner, T., 2015. A continental-weathering control on orbitally driven
801   redox-nutrient cycling during Cretaceous Oceanic Anoxic Event 2. Geology 43, 963–
802   966. doi:10.1130/G36837.1

803   Raiswell, R., Hardisty, D.S., Lyons, T.W., Canfield, D.E., Owens, J.D., Planavsky, N.J.,
804   Poulton, S.W., Reinhard, C.T., 2018. The iron paleoredox proxies: A guide to the
805   pitfalls, problems and proper practice. American Journal of Science 318, 491–526.
806   doi:10.2475/05.2018.03

807   Raven, M.R., Fike, D.A., Gomes, M.L., Webb, S.M., Bradley, A.S., McClelland, H.-
808   L.O., 2018. Organic carbon burial during OAE2 driven by changes in the locus of
809   organic matter sulfurization. Nature Communications 9, 3409. doi:10.1038/s41467-
810   018-05943-6

811   Raven, M.R., Sessions, A.L., Adkins, J.F., Thunell, R.C., 2016a. Rapid organic matter
812   sulfurization in sinking particles from the Cariaco Basin water column. Geochimica
813   et Cosmochimica Acta 190, 175–190. doi:10.1016/j.gca.2016.06.030

814   Raven, M.R., Sessions, A.L., Fischer, W.W., Adkins, J.F., 2016b. Sedimentary pyrite δ
815   34 S differs from porewater sulfide in Santa Barbara Basin: Proposed role of organic
816   sulfur. Geochimica et Cosmochimica Acta 186, 120–134.
817   doi:10.1016/j.gca.2016.04.037

818   Sageman, B.B., Meyers, S.R., Arthur, M.A., 2006. Orbital time scale and new C-isotope
819   record for Cenomanian-Turonian boundary stratotype. Geology 34, 125–4.
820   doi:10.1130/G22074.1

821   Vairavamurthy, A., 1998. Using X-ray absorption to probe sulfur oxidation states in
822   complex molecules. Spectrochimica Acta Part A: Molecular and … 54, 2009–2017.
823   doi:10.1016/S1386-1425(98)00153-X

824   van Dongen, B.E., Schouten, S., Baas, M., Geenevasen, J.A.J., Sinninghe Damsté, J.S.,
825   2003. An experimental study of the low-temperature sulfurization of carbohydrates.
826   Organic Geochemistry 34, 1129–1144. doi:10.1016/S0146-6380(03)00060-3

827   Vivier, Du, A.D.C., Selby, D., Sageman, B.B., Jarvis, I., Gröcke, D.R., Voigt, S., 2014.
828   Marine 187Os/188Os isotope stratigraphy reveals the interaction of volcanism and
829   ocean circulation during Oceanic Anoxic Event 2. Earth and Planetary Science
830   Letters 389, 23–33. doi:10.1016/j.epsl.2013.12.024

831   Wan, M., Schröder, C., Peiffer, S., 2017. Fe (III): S (-II) Concentration Ratio Controls the
832   Pathway and the Kinetics of Pyrite Formation during Sulfidation of Ferric
833   Hydroxides. Geochimica et Cosmochimica Acta. doi:10.1016/j.gca.2017.08.036

834   Webb, S.M., 2005. SIXpack: a graphical user interface for XAS analysis using IFEFFIT.
835   Phys. Scr. 2005, 1011. doi:10.1238/Physica.Topical.115a01011

836   Wenk, C.B., Wing, B.A., Halevy, I., 2017. Electron carriers in microbial sulfate reduction
837   inferred from experimental and environmental sulfur isotope fractionations 1–13.
838   doi:10.1038/ismej.2017.185

839   Werne, J.P., Lyons, T.W., Hollander, D.J., Chemical, M.F., Sinninghe Damsté, J.S.,

840   2003. Reduced sulfur in euxinic sediments of the Cariaco Basin: sulfur isotope
841   constraints on organic sulfur formation. Chemical Geology 195, 159–179.
842   doi:10.1016/S0009-2541(02)00393-5
843